

Supporting Information

Efficient green electroluminescence based on an iridium(III) complex with different device structures

Yi-Ming Jing,^a You-Xuan Zheng,^{a,b,c,*} Jing-Lin Zuo^a

^a State Key Laboratory of Coordination Chemistry, Collaborative Innovation Center of Advanced Microstructures, School of Chemistry and Chemical Engineering, Nanjing University, Nanjing 210093, P. R. China, e-mail: yxzheng@nju.edu.cn

^b MaAnShan High-Tech Research Institute of Nanjing University, MaAnShan, 238200, P. R. China

^c State Key Laboratory of Luminescence and Applications, Changchun Institute of Optics, Fine Mechanics and Physics, Chinese Academy of Science, Changchun 130033, P. R. China

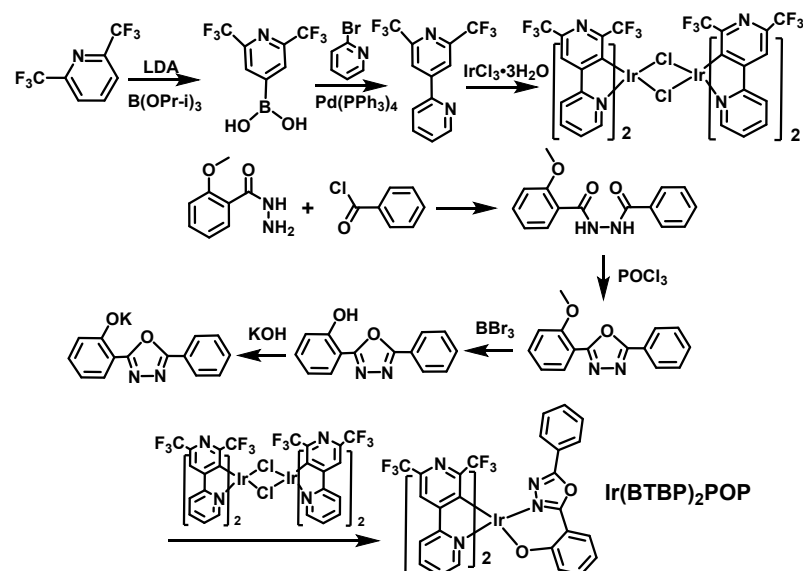
Experimental section

Materials and measurements

All the organic materials used in this study were obtained commercially and used as received without further purification except for Ir(BTBP)₂POP, which was synthesized and purified in our laboratory. ¹H and ¹⁹F NMR spectra were measured on a Bruker AM 500 spectrometer. Electrospray ionization mass spectra (ESI-MS) were obtained with ESI-MS (LCQ Fleet, Thermo Fisher Scientific). The high resolution mass spectra (HR EI-MS) were recorded on an Agilent 6540 UHD Accurate-Mass Q-TOF LC/MS. Elemental analyses for C, H and N were performed on an Elementar Vario MICRO analyzer. TG-DSC measurements were carried out on a DSC 823e analyzer (METTLER). UV-vis absorption and photoluminescence (PL) spectra were measured on a Shimadzu UV-3100 and a Hitachi F-4600 spectrophotometer at room temperature, respectively. The luminescence quantum efficiencies were calculated by a comparison of the emission intensities (integrated areas) of a standard sample *fac*-Ir(ppy)₃ and the unknown samples in deaerated CH₂Cl₂ solutions of 5 × 10⁻⁵ mol L⁻¹. Cyclic voltammetry measurements were conducted on a MPI-A multifunctional electrochemical and chemiluminescent system (Xi'an Remex Analytical Instrument Ltd. Co., China) at room temperature, with a polished Pt plate as the working

electrode, platinum thread as the counter electrode and Ag-AgNO₃ (0.1 M) in CH₃CN as the reference electrode, *tetra*-*n*-butylammonium perchlorate (0.1 M) was used as the supporting electrolyte, using Fc⁺/Fc as the internal standard, the scan rate was 0.05 V/s.

Syntheses



Scheme S1. Synthetic routes of ligands and the complex.

Scheme S1 shows the chemical structure of the **Ir(BTBP)₂POP** complex. The cyclometallated ligand (2',6'-bis(trifluoromethyl)-2,4'-bipyridine, BTBP), cyclometallated Ir(III) chloro-bridged dimer ($[(\text{BTBP})_2\text{Ir}(\mu\text{-Cl})]_2$) and the ancillary ligand (HPOP) were synthesized according to our previous report.² All reactions were performed under nitrogen. Solvents were carefully dried and distilled from appropriate drying agents prior to use.

General syntheses of Ir(BTBP)₂POP

The chloro-bridged dimer ($[(\text{BTBP})_2\text{Ir}(\mu\text{-Cl})]_2$, 0.2 mmol) and the ancillary potassium salt (KPOP, 0.5 mmol) in 2-ethoxyethanol (20 mL) was refluxed for 24 h. After the mixture was cooled, the solvent was evaporated at low pressure. The crude product was washed by water, and the column chromatography using CH₂Cl₂ as the eluent gave the complex which was further purified again by sublimation in vacuum.

Ir(BTBP)₂POP (yield: 53%): ¹H NMR (300 MHz, CDCl₃) δ 8.70 (d, *J* = 5.6 Hz, 1H), 8.10 (t, *J* = 7.9 Hz, 3H), 8.04 (s, 1H), 7.85 (t, *J* = 7.7 Hz, 2H), 7.74 (d, *J* = 7.1 Hz, 2H), 7.57 (dd, *J* = 10.2, 7.7 Hz, 2H), 7.49 (t, *J* = 7.3 Hz, 3H), 7.20 (d, *J* = 6.6 Hz, 2H), 7.01 (t, *J* = 6.6 Hz, 1H), 6.63 (d, *J* = 8.4 Hz, 1H), 6.52 (t, *J* = 7.4 Hz, 1H). ¹⁹F NMR (400 MHz, CDCl₃) δ -63.60 (s, 3F), -64.12 (s, 3F), -67.28 (s, 3F), -67.44 (s, 3F). HR EI-MS *m/z* calcd for C₃₈H₁₉F₁₂IrN₆O₂: 1012.1085, found: 1013.1081 [M+H]⁺. Anal. Calcd. For C₃₈H₁₉F₁₂IrN₆O₂: C, 45.11; H, 1.89; N, 8.31. Found: C, 45.06; H, 1.92; N, 8.33.

Thermal stability

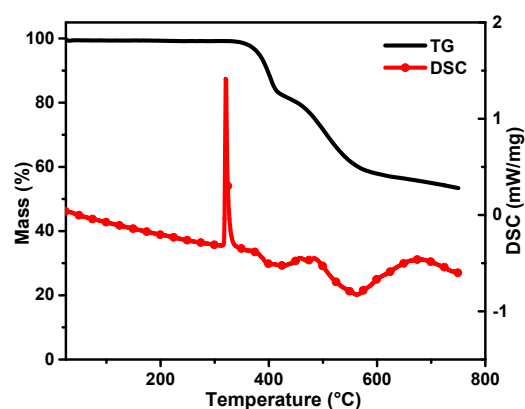


Fig. S1. TG and DSC thermograms of $\text{Ir}(\text{BTBP})_2\text{POP}$.

The thermal stability of the emitters is important for the stability of OLEDs. The thermal properties of $\text{Ir}(\text{BTBP})_2\text{POP}$ were characterized by thermogravimetric (TG) and differential scanning calorimetry (DSC) measurements under a nitrogen stream. From the DSC curve in Fig. S1 it can be observed that the melting point of $\text{Ir}(\text{BTBP})_2\text{POP}$ is as high as 320 °C. The TG curve gives the decomposition temperature (5% loss of weight) of 382 °C for $\text{Ir}(\text{BTBP})_2\text{POP}$. Furthermore, the complex can be vacuum evaporated easily without decomposition and shows good film-forming ability, which indicates that the complex is potential emitting material for the fabrication of stable OLEDs.

Photophysical property

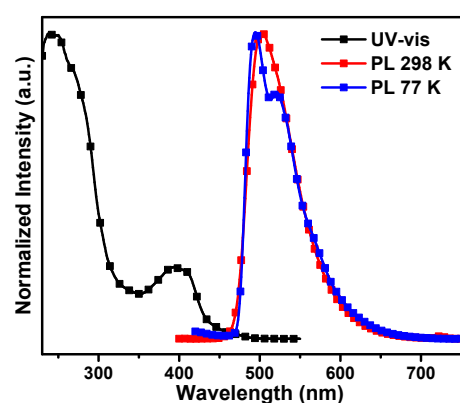


Fig. S2. Normalized UV-vis absorption and emission spectra of $\text{Ir}(\text{BTBP})_2\text{POP}$ in degassed CH_2Cl_2 solutions ($5 \times 10^{-5} \text{ mol} \cdot \text{L}^{-1}$) at room temperature and 77 K.

The UV-vis absorption spectra of the **Ir(BTBP)₂POP** complex in degassed CH₂Cl₂ at 5×10^{-5} mol·L⁻¹ is shown in Fig. S2 and the physical data are listed in Table S1. The intense bands at high energy (230-350 nm) are assigned to the spin-allowed ligand-centered ¹LC (π - π^*) transition of the cyclometalated primary ligand (BTBP) and the ancillary ligand. The relatively weak absorption bands at lower energies extending into the spectral region (350-500 nm) are attributed to the mixing of the spin-allowed singlet metal-to-ligand charge-transfer (¹MLCT) and triplet metal-to-ligand charge-transfer (³MLCT) states, or LLCT (ligand-to-ligand charge-transfer) transition through strong spin-orbit coupling of iridium atoms.³ Photoluminescence measurements were conducted in deaerated CH₂Cl₂ solutions at room temperature and 77 K (Fig. S2 and Table S1). Under the excitation of 393 nm, **Ir(BTBP)₂POP** complex emitted green phosphorescence in CH₂Cl₂ at room temperature with the peak maxima at 503 nm. Moreover, the quantum yield of the complex in solution is 88.25%.

As shown in Fig. S2, the structured emission at 77 K reveals that the mixing between the ³MLCT and the LLCT levels is so effective that an almost ligand-centered emission is observed upon freezing of the matrix. The rigidity of the solvent dramatically affects the stabilization of the charge-transfer states, which shift to higher energy at low temperature, and the electronic mixing of the two states decreases.

The phosphorescence lifetime (τ) is the crucial factor that determines the rate of triplet-triplet annihilation in OLEDs. Longer τ values usually cause greater triplet-triplet annihilation.⁴ The lifetimes of **Ir(BTBP)₂POP** is in the range of microseconds (2.86 μ s in CH₂Cl₂ solution) at room temperature (Table S1) and is indicative of the phosphorescent origin for the excited states.

Table S1. Physical data of **Ir(BTBP)₂POP**.

Complex	T_m/T_d ^{a)} (°C)	λ_{abs} ^{b)} (nm)	λ_{em} ^{c)} (nm)		Φ_p ^{d)} (%)	τ ^{e)} (μ s)	HOMO/LUMO ^{f)} (eV)
			298 K	77 K			
Ir(BTBP)₂POP	320/382	238, 258, 393	503	494, 521	88.25	2.86	-5.93/-2.76

^{a)} T_m : melting temperature, T_d : decomposition temperature; ^{b)} Measured in degassed CH₂Cl₂ solution at a concentration of 5×10^{-5} mol·L⁻¹ at room temperature; ^{c)} Measured in degassed CH₂Cl₂ solution at a concentration of 5×10^{-5} mol·L⁻¹ at 298 and 77 K, respectively; ^{d)} Measured in degassed CH₂Cl₂ solution at room temperature using *fac*-Ir(ppy)₃ as the standard sample ($\Phi = 0.4$). ^{e)} Measured in degassed CH₂Cl₂ solution at a concentration of 5×10^{-5} mol·L⁻¹ at room temperature; ^{f)} From the onset of oxidation

potentials of the cyclic voltammetry (CV) diagram using ferrocene as the internal standard and the optical band gap from the absorption spectra in degassed solution (CH_2Cl_2 : CH_3CN = 1: 1).

Since $\text{Ir}(\text{BTBP})_2\text{POP}$ existed in films in OLEDs, the UV-vis absorption and emission spectra of the complex in films of different host materials with different doping concentration (0, 6, 8, 10, 100 wt%) were carried out and shown in Fig. S3. From the UV-vis absorption spectra of $\text{Ir}(\text{BTBP})_2\text{POP}$ in films of mCP (Fig. S3 (a)) and PPO21 (Fig. S3 (b)) with different doping concentration, it can be figured out that the absorption peaks at lower energies extending into the spectral region (360-500 nm) rise as the doping concentration increases, and the absorption spectra are similar to those in degassed solution (Fig. S2) when the films are consisted of $\text{Ir}(\text{BTBP})_2\text{POP}$ with 100 wt% doping concentration. On the other hand, the intense bands at high energy (230-360 nm) of the absorption spectra in the films with the doping concentration of 6, 8 and 10 wt% are similar, which are attributed to the mixing of the relevant absorption bands of host materials and $\text{Ir}(\text{BTBP})_2\text{POP}$.

The emission spectra of films with different doping concentration of $\text{Ir}(\text{BTBP})_2\text{POP}$ (6, 8, 10, 100 wt%) were measured under the excitation of 393 nm, which were also depicted in Fig. S3. Films of 6, 8 and 10 wt% doping concentration have almost the same emission spectra with a maximum peak (496 – 498 nm) similar to the EL spectra of OLEDs. The absence of mCP or PPO21 emission suggests a complete energy transfer from the host to the dopant excited by photons. A peak maxima at 516 nm was found in the emission spectrum of the film of $\text{Ir}(\text{BTBP})_2\text{POP}$ without doping, which was red shifted compared with the PL spectrum in degassed solution at room temperature caused by the interactions of molecules in the solid state.

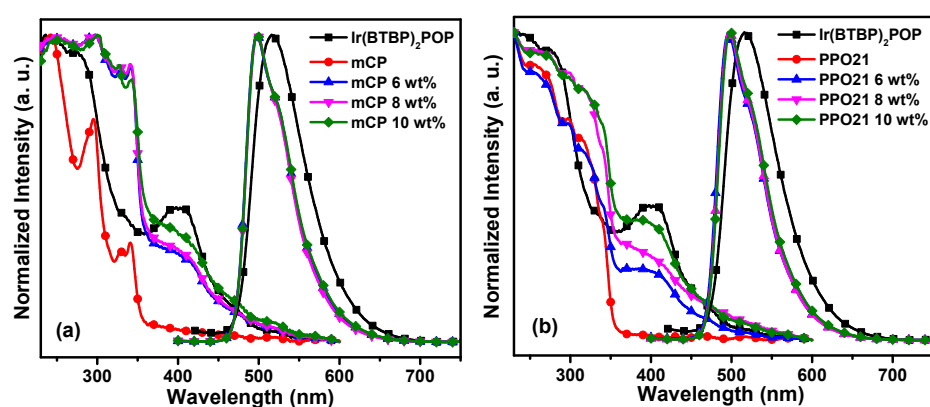


Fig. S3. Normalized UV-vis absorption and emission spectra of $\text{Ir}(\text{BTBP})_2\text{POP}$ in films of mCP (a) and PPO21 (b) with different doping concentration.

Electrochemical properties and theoretical calculation

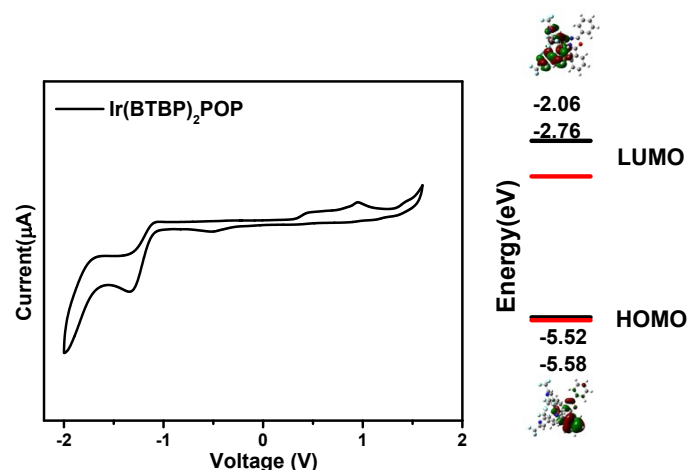


Fig. S4. Cyclic voltammogram curve (left) and contour plots of HOMO/LUMO with theoretical (black) and experimental (red) energy levels (right) of **Ir(BTBP)₂POP**.

The redox properties and HOMO/LUMO energy levels of the dopants are relative to the charge transport ability and the OLED structure. In order to calculate the HOMO and LUMO energy levels of the complex, the electrochemical properties of **Ir(BTBP)₂POP** were measured by cyclic voltammetry in deaerated solution (CH_2Cl_2 : $\text{CH}_3\text{CN} = 1: 1$) (Fig. S5 (left)). The HOMO level was calculated from the oxidation peak potential (E_{ox}) and the band gap (E_{g}) was calculated from the UV-vis absorption edges.⁸ Then the LUMO level was determined according to the equation $\text{LUMO} = \text{HOMO} + E_{\text{g}}$. The electrochemical data are collected in Table S4. The cyclic voltammograms of the complex in the positive range show strong oxidation peaks, while the reduction peaks are not obvious, demonstrating that the redox process of the complex is not reversible completely, which is also observed in related Ir(III) complexes containing oxadiazole units.⁹ In the negative potential scan range the complex exhibits quasi-reversible oxidation and reduction process due to the 1,3,4-oxadiazol substituent suggesting the electron-transporting and electron trapping characteristics. From Fig. S5 and Table S4, it can be observed that the HOMO and LUMO levels of **Ir(BTBP)₂POP** are -5.58 eV and -2.76 eV, respectively.

For providing further study of the electronic structures of the complex, the theoretical calculation was performed on optimized geometries in CH_2Cl_2 . The calculations on the ground electronic states of the complexes were carried out using density functional theory (DFT) and time-dependent DFT (TD-DFT) at the B3LYP level.¹⁰ The basis set used for C, H, N, O, F and S atoms was 6-31G(d, p) while the LanL2DZ basis set was used for Ir atoms.¹¹ The solvent effect of CH_2Cl_2 was taken into consideration using conductor-like polarizable continuum model (C-PCM).¹² All these calculations were performed with Gaussian 09.¹³ QMForge program was used to give accurate

percentage data of FMOs. Contour plots of the frontier molecular orbitals (FMOs) are shown in Fig. S5 (right). The energies and percentage composition of ligand and metal orbitals are shown in Table S5. The results are helpful for the assignment of the electron transition characteristics and the discussion on the photophysical variations. According to Fig. S5 (right) and Table S5, it is obviously that the HOMO corresponds to a mixture of the *d* orbitals of Ir (15.56 %) and the π orbitals of the phenyl ring of the ancillary ligand (77.69 %) with minor contribution from the BTBP ligand (6.75 %). The oxidation processes occurred with metal centered orbitals and a contribution from the phenyl ring of ancillary ligands.¹⁹ On the other hand, the LUMO level of **Ir(BTBP)₂POP** is mainly located on the primary ligand (BTBP) with the composition of 94.38 %, while the ratio on the ancillary ligand is as low as 2.75 %.

Table S2. Electrochemical data of **Ir(BTBP)₂POP**.

Complex	E_{ox} (V) ^{a)}	E_{red} (V)	HOMO (eV) ^{b)}	LUMO (eV)	E_g (eV)
Ir(BTBP)₂POP	0.95	-1.34	-5.58	-2.76	2.82

^{a)} Oxidation potential measured in solution at 0.05 mV/s.

^{b)} The HOMO energy levels were calculated from the equation: HOMO (eV) = $E_{\text{ox}} - E_{\text{Fc}^+/\text{Fc}} + 4.8$.

Table S3. Percentage distributions of HOMO and LUMO in **Ir(BTBP)₂POP**.

Complex	Orbital	Energy/eV (Calculated)	E_{gap} /eV (Calculated)	Composition (%)		
				Ir	BTBP	LX
Ir(BTBP)₂POP	HOMO	-5.517	3.451	15.56	6.75	77.69
	LUMO	-2.065		2.86	94.38	2.75

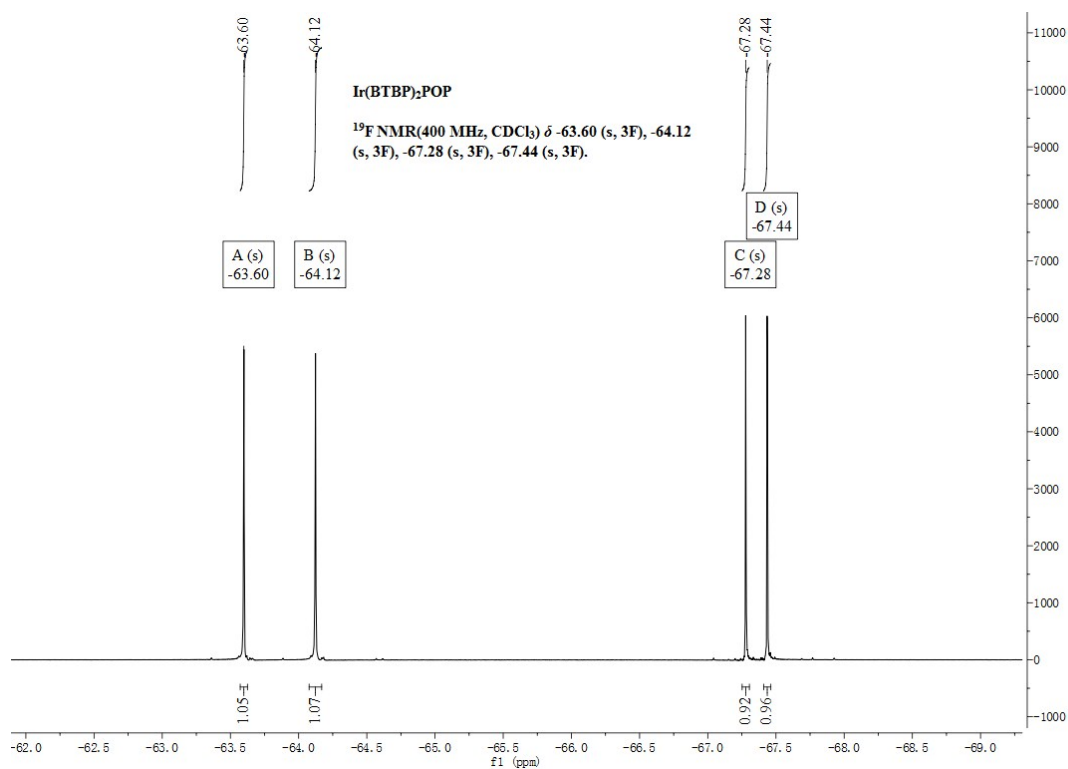


Fig. S5. ^{19}F NMR spectrum of $\text{Ir}(\text{BTBP})_2\text{POP}$.

Notes and references

^a State Key Laboratory of Coordination Chemistry, Collaborative Innovation Center of Advanced Microstructures, School of Chemistry and Chemical Engineering, Nanjing University, Nanjing 210093, P. R. China, e-mail: yxzheng@nju.edu.cn

^b MaAnShan High-Tech Research Institute of Nanjing University, MaAnShan, 238200, P. R. China

^c State Key Laboratory of Luminescence and Applications, Changchun Institute of Optics, Fine Mechanics and Physics, Chinese Academy of Science, Changchun 130033, P. R. China

- (a) A. Juris, V. Balzani, F. Barigelletti, S. Campagna, P. Belser and A. von Zelewsky, *Coord. Chem. Rev.*, 1988, **84**, 85; (b) K. A. King, P. J. Spellane and R. J. Watts, *J. Amer. Chem. Soc.*, 1985, **107**, 1431.
- (a) Y.-M. Jing, C.-C. Wang, L.-S. Xue, T.-Y. Li, S. Zhang, X. Liu, X. Liang, Y.-X. Zheng and J.-L. Zuo, *J. Organomet. Chem.*, 2014, **765**, 39; (b) H.-Y. Li, T.-Y. Li, M.-Y. Teng, Q.-L. Xu, S. Zhang, Y.-M. Jin, X. Liu, Y.-X. Zheng and J.-L. Zuo, *J. Mater. Chem. C*, 2014, **2**, 1116; (c) X. Liu, S. Zhang, Y.-M. Jin, G.-Z. Lu, L. Jiang, X. Liang, Q.-L. Xu and Y.-X. Zheng, *J. Organomet. Chem.*, 2015, **785**, 11-18.
- (a) Y. Tao, C. Yang and J. Qin, *Chem. Soc. Rev.*, 2011, **40**, 2943; (b) T. Hofbeck and H. Yersin, *Inorg. Chem.*, 2010, **49**, 9290; (c) E. E. Langdon-Jones, A. J. Hallett, J. D. Routledge, D. A. Crole, B. D. Ward, J. A. Platts and S. J. Pope, *Inorg. Chem.*, 2012, **52**, 448; (d) S.-K. Leung, K. Y. Kwok, K. Y. Zhang and K. K.-W. Lo, *Inorg. Chem.*, 2010, **49**, 4984; (e) M. Tavasli, T. N. Moore, Y. Zheng, M. R.

- Bryce, M. A. Fox, G. C. Griffiths, V. Jankus, H. A. Al-Attar and A. P. Monkman, *J. Mater. Chem.*, 2012, **22**, 6419.
4. (a) M. A. Baldo, C. Adachi and S. R. Forrest, *Phys. Rev. B*, 2000, **62**, 10967; (b) E. B. Namdas, A. Ruseckas, I. D. Samuel, S.-C. Lo and P. L. Burn, *Appl. Phys. Lett.*, 2005, **86**, 91104.
5. *SAINT-Plus, version 6.02*, Bruker Analytical X-ray System, Madison, WI, 1999.
6. G. M. Sheldrick, *SADABS An empirical absorption correction program*, Bruker Analytical X-ray Systems, Madison, WI, 1996.
7. G. M. Sheldrick, *SHELXTL-97*, Universität of Göttingen, Göttingen, Germany, 1997.
8. P. Brulatti, R. J. Gildea, J. A. Howard, V. Fattori, M. Cocchi and J. G. Williams, *Inorg. Chem.*, 2012, **51**, 3813.
9. (a) L.Q. Chen, C. L. Yang, M. Li, J. G. Qin, J. Gao, H. You and D.G. Ma, *Crystal Growth & Design*, 2007, **7**, 39; (b) L. Q. Chen, H. You, C. L. Yang, D. G. Ma and J. G. Qin, *Chem. Comm.*, 2007, **13**, 1352; (c) Z. W. Xu, Y. Li, X. M. Ma, X. D. Gao and H. Tian, *Tetrahedron*, 2008, **64**, 1860; (d) Y. H. Zheng, A. S. Batsanov and M. R. Bryce, *Inorg. Chem.*, 2011, **50**, 3354.
10. (a) B. W. D'Andrade, S. Datta, S. R. Forrest, P. Djurovich, E. Polikarpov and M. E. Thompson, *Org. Electron.*, 2005, **6**, 11; (b) E. Runge and E. K. U. Gross, *Phys. Rev. Lett.*, 1984, **52**, 997; (c) A. D. Becke, *J. Chem. Phys.*, 1993, **98**, 5648; (d) C. Lee, W. Yang and R. G. Parr, *Phys. Rev. B*, 1988, **37**, 785.
11. (a) M. M. Francl, W. J. Pietro, W. J. Hehre, J. S. Binkley, M. S. Gordon, D. J. DeFrees and J. A. Pople, *J. Chem. Phys.*, 1982, **77**, 3654; (b) P. J. Hay and W. R. Wadt, *J. Chem. Phys.*, 1985, **82**, 299.
12. V. Barone and M. Cossi, *J. Phys. Chem. A*, 1988, **102**, 1995.
13. M. J. Frisch, G. W. Trucks, H. B. Schlegel, G. E. Scuseria, M. A. Robb, J. R. Cheeseman, G. Scalmani, V. Barone, B. Mennucci, G. A. Petersson, H. Nakatsuji, M. Caricato, X. Li, H. P. Hratchian, A. F. Izmaylov, J. Bloino, G. Zheng, J. L. Sonnenberg, M. Hada, M. Ehara, K. Toyota, R. Fukuda, J. Hasegawa, M. Ishida, T. Nakajima, Y. Honda, O. Kitao, H. Nakai, T. Vreven, J. A. Montgomery Jr., J. E. Peralta, F. Ogliaro, M. Bearpark, J. J. Heyd, E. Brothers, K. N. Kudin, V. N. Staroverov, R. Kobayashi, J. Normand, K. Raghavachari, A. Rendell, J. C. Burant, S. S. Iyengar, J. Tomasi, M. Cossi, N. Rega, J. M. Millam, M. Klene, J. E. Knox, J. B. Cross, V. Bakken, C. Adamo, J. Jaramillo, R. Gomperts, R. E. Stratmann, O. Yazyev, A. J. Austin, R. Cammi, C. Pomelli, J. W. Ochterski, R. L. Martin, K. Morokuma, V. G. Zakrzewski, G. A. Voth, P. Salvador, J. J. Dannenberg, S. Dapprich, A. D. Daniels, O. Farkas, J. B. Foresman, J. V. Ortiz, J. Cioslowski and D. J. Fox, *Gaussian 09, Revision A.01*, Gaussian, Inc., Wallingford, CT, **2009**.
14. (a) C. Dragonetti, L. Falciola, P. Mussini, S. Righetto, D. Roberto, R. Ugo and A. Valore, *Inorg. Chem.*, 2007, **46**, 8533; (b) J. Zhang, L. Zhou, H. A. Al-Attar, K. Shao and L. Wang, *Adv. Funct. Mater.*, 2013, **23**, 4667.